Calculation of tip-enhanced Raman spectra of carbon nanostructures

Fadel, Mayada; Henrard, Luc; Meunier, Vincent

Published in:
Carbon Trends

DOI:
10.1016/j.cartre.2023.100286

Publication date:
2023

Document Version
Publisher's PDF, also known as Version of record

Carbon Trends 12 (2023) 100286

Contents lists available at ScienceDirect

Carbon Trends

journal homepage: www.elsevier.com/locate/cartre

Calculation of tip-enhanced Raman spectra of carbon nanostructures

Mayada Fadel [a], Luc Henrard [b], Vincent Meunier [c,*]

[a] Department of Physics, Applied Physics, and Astronomy, Rensselaer Polytechnic Institute, Troy, NY, USA
[b] Department of Physics, Namur Institute of Structured Matter, University of Namur, Namur, Belgium
[c] Department of Engineering Science and Mechanics, The Pennsylvania State University, State College, PA, USA

A B S T R A C T

An efficient semiempirical computational methodology is developed for the simulation of Tip-Enhanced Raman Spectroscopy (TERS), by combining the discrete-dipole approximation (DDA), the bond polarizability model (BPM), and density functional theory (DFT) to describe the vibrational properties of the material system. The method is illustrated for C_{60} whose TERS spectra are determined for different frequencies of incident illumination and for different tip shapes. The information on the local properties of the structure is correlated with the computed TERS signature, which is obtained by scanning the tip over the molecule. The method is versatile and is found to have a modest computational cost while allowing one to highlight the main features differentiating TERS from conventional Raman spectroscopy.

1. Introduction

Raman spectroscopy is an analytical tool used to study intrinsic vibrations for the identification and characterization of materials. Each material has its own unique Raman spectrum that therefore constitutes its specific fingerprint. Additionally, a Raman spectrum can be used to track structural or chemical changes since the vibrations are sensitive to the various modifications of the way atoms are bonded and arranged, at local or global scales. Although Raman is a powerful nondestructive tool, its signal is very weak. As a result, research has been performed to develop ways to enhance the signal intensity. Raman spectroscopy involves the coupling of a material's intrinsic properties (i.e., atomic and electronic structures) with an external electromagnetic field (i.e., laser light). One way to increase the intensity of the signal is to create a nanocavity in the vicinity of the material system by placing it in the proximity of a noble-metal nanoparticle. In the Raman scattering of a molecule, the intensity of the photonic absorption process is directly proportional to the intensity of the local electric field [1], and the enhancement is essentially due to a local increase in the electric field. In general, there exist two distinct enhancement mechanisms: electromagnetic and chemical. In electromagnetic enhancement, the excitations of the nanoparticle plasmons amplify the local field, resulting in an increase in the photon absorption process, which in turn leads to an enhancement of the Raman signal, while the chemical enhancement is due to charge transfer [1]. Here, we will focus on the electromagnetic enhancement process.

When the target molecule is adsorbed onto a metal nanoparticle, the physical enhancement process is known as surface-enhanced Raman spectroscopy (SERS) with a reported enhancement factor of $10^{10} - 10^{14}$ [2]. Alternatively, the target molecule can be placed in the vicinity of a nanoparticle used as a probing tip, leading to a distinct technique known as *tip-enhanced Raman spectroscopy* (TERS) with a reported enhancement factor of $10^3 - 10^6$ [2]. The enhancement factor provided by TERS is generally weaker than that of SERS. This can be understood as follows: In TERS, there is only one single nanoparticle that is the source of enhancement, while in SERS there are multiple nanoparticles and multiple gaps between them called hot spots, and these hot spots contribute more to electromagnetic enhancement [2]. Additionally, the chemical enhancement in SERS is greater than that in TERS due to the possible adsorption of the molecule on the nanoparticles in SERS [2–4]. In TERS, Raman spectroscopy is combined with a scanning probe technique such as *scanning tunneling microscopy* (STM) [5] or *atomic force microscopy* (AFM) [6]. The electric field generated from the tip is enhanced and localized, which provides high spatial resolution. Moving the tip, which is the enhancement source in TERS, allows for control of the localization of the field acting on the target, which provides additional information beyond a conventional Raman spectrum, including knowledge related to the local density of the phonon states [7]. The first TERS experiment was demonstrated in 2000 by Stöckle et al. [8] using

* Corresponding author.
E-mail address: mayada.m.fadel@gmail.com (M. Fadel).

https://doi.org/10.1016/j.cartre.2023.100286
Received 1 June 2023; Received in revised form 18 July 2023; Accepted 20 July 2023
Available online 26 July 2023

AFM-TERS, followed by a number of other studies including those of Anderson [9], Pettinger et al. [10] and Hayazawa et al. [11].

Under a homogeneous electric field, the selection rule for Raman-active vibrations is due to non-zero changes in the polarizability of the molecule or solid with respect to the normal modes of vibration. The selection rule assumes a homogeneous electric field and, as a result, can be solely determined based on the symmetry of the Raman tensor (which is itself obtained from inspection of the character table of the structure's point group symmetry). In contrast, in the case of TERS, these selection rules are no longer valid as the field generated at the tip is spatially inhomogeneous, which means that different atoms in the molecule are subjected to a different field [12,13]. This leads to changes in the relative Raman cross section of the normal modes, and even sometimes to a modification in the normal modes themselves.

To simulate TERS, one needs to compute the optical response of the molecule and the nanoparticle, in addition to their coupling. This involves the interplay of several degrees of freedom: electromagnetic, electronic, vibrational, and dielectric. In a recent publication (Ref. [14]), the authors developed a general method to compute the TERS of single molecules. They calculated the optical response of the nanoparticle and the polarizability of the target molecule separately, and then combined them to obtain the Raman intensities under an inhomogeneous electric field. Calculating the localized near-field of the nanoparticle at the tip apex requires the implementation of a method that takes into consideration the atomic nature of the nanoparticle and the target molecule [14]. To tackle this, here we choose to adopt the classical *discrete-dipole approximation* (DDA) [15,16]. Additionally, for the calculation of the TERS cross section, we use the *bond polarizability method* (BPM) to calculate the polarizability derivatives with respect to the normal modes, since this method has shown to compare qualitatively favorably with more advanced methods [17,18]. Finally, a finite-difference scheme (as implemented in Phonopy [19]) is used to calculate the normal modes and their corresponding frequencies using *density functional theory* (DFT) to calculate the force constants. In this work, we have developed this theory to compute TERS spectra for buckminsterfullerene (C_{60}) placed in the proximity of a silver tetrahedron-shaped nanoparticle. We also show how the method is used to raster the silver nanoparticle around the molecule to produce TERS scans of C_{60} for different normal modes.

2. Theoretical formulation

There are a number of different properties involved in the calculation of a TERS spectrum. First, let us outline the semiclassical formulation of Raman scattering (*that is*, where the electromagnetic field is treated classically). In the usual Raman scattering, where the field acting on a target molecule with $\mathcal{N}$ atoms is homogeneous, the familiar semi-classical expression of the intensity of the Stokes Raman process [17] is given by

$$I(\omega) \propto \omega_{\text{inc}} \omega_{\text{S}}^3 \sum_{\upsilon=1}^{3\mathcal{N}} (\langle n(\omega_\upsilon)\rangle + 1) \left| \boldsymbol{\eta}' \cdot \bar{\alpha}_\upsilon^{\text{Ram}} \cdot \mathbf{E}^{\text{inc}} \right|^2 \delta(\omega - \omega_\upsilon), \tag{1}$$

where

$$\bar{\alpha}_\upsilon^{\text{Ram}} = \frac{1}{2} \left(\frac{\partial \bar{\alpha}}{\partial \mathbf{Q}_\upsilon} \right)_0 \mathbf{Q}_{\upsilon 0}. \tag{2}$$

$\mathbf{Q}_\upsilon = \mathbf{Q}_{\upsilon 0} \cos(\omega_\upsilon t + \delta_\upsilon)$ is one of the $3\mathcal{N}$ normal modes of vibration with displacement $\mathbf{Q}_{\upsilon 0}$, phase shift δ_υ, and frequency ω_υ. The frequencies of incident and scattered monochromatic lights are ω_{inc} and ω_{S}, respectively. $\langle n(\omega_\upsilon)\rangle = 1/(\exp(\hbar\omega_\upsilon/k_{\text{B}}T) - 1)$ is the Bose-Einstein occupation of mode υ at temperature T. $\boldsymbol{\eta}'$ is the direction of polarization of scattered light; $\mathbf{E}^{\text{inc}}$ is the incident electric field; and $\bar{\alpha}_\upsilon^{\text{Ram}}$ is the Raman tensor of mode υ, which is defined by the derivatives of the polarizability of the molecule with respect to the vibrational mode υ. When evaluating a TERS spectrum within the semiclassical theory, the only term that needs to be modified is the one between the || symbol. This is due to the fact that in TERS, the incident electric field $\mathbf{E}^{\text{inc}}$ is no longer homogeneous over all of the atoms in the molecule, in contrast to conventional Raman. Note that in normal Raman scattering, the electric field strength can be factored out and the selection rules are directly related to the symmetry of the Raman tensor (Eq. (2)).

The workflow of the calculation of the TERS spectrum includes the computation of the vibrational modes and the corresponding frequencies of the molecule, the polarizability derivatives with respect to the normal modes, and the inhomogeneous field at the tip (due to the application of an external electric field).

In this work, we use a combination of approaches to evaluate the salient properties needed to describe TERS. First, we carry out the phonon calculation using Phonopy [19]; an open source package to calculate phonons within the harmonic and quasi-harmonic approximations. Phonopy is paired with a calculator for the computation of the atomic forces obtained within a finite displacement scheme. Here, we use DFT to evaluate the forces, using the Hellman-Feynman theorem. Specifically, we employ the GPAW package [20,21], which is a Python code based on the projector-augmented wave (PAW) method and the atomic simulation environment (ASE) [22]. In this study, we approximate the exchange-correlation potential with the Perdew-Burke-Ernzerhof (PBE) functional [23] and we expand the wave functions on a plane-wave basis with an energy cutoff of 450 eV. The molecule is relaxed to the point that all atomic forces are below 0.01 eV/Å before proceeding with the calculation of the phonons. Second, we use the bond polarizability method (BPM) [17,18] to calculate the derivatives of polarizability with respect to the normal modes. Third, we compute the localized near-field at the apex of the nanoparticle (modeled as a tetrahedron of silver atoms) at the tip apex using the discrete-dipole approximation (DDA) [14]. Finally, we obtain the TERS spectra of the target molecule using Eq. (1).

Before moving on to the application of this scheme to the TERS spectrum of the C_{60} molecule, we will first describe the DDA and BPM methods.

2.1. Discrete dipole approximation

According to Maxwell's equations, when a nanoparticle is subjected to an incident electric field $\mathbf{E}^{\text{inc}}$, the free carriers in the particle rearrange to minimize the effective field inside the metal. This can lead to a very large increase in the local field right outside the tip, especially for sharp protrusions, as predicted by classical electromagnetic theory. There are several different ways to account for this effect. Here, we calculate the induced electric field from the tip within the DDA [14], which can be used to obtain the absorption, scattering, and enhanced field around a nanoparticle of arbitrary shape and composition [24]. This method was initially proposed by Purcell and Pennypacker for the calculation of the absorption and scattering of dielectric grains in interstellar matter [16]. In DDA, a cubic mesh is created to represent the nanoparticle, such that it is divided into $\mathcal{M}$ nanocubes. Each cube represents a point dipole such that the nanoparticle is described by a set of $\mathcal{M}$ point dipoles that interact with each other [16,24]. The electric field acting on each dipole is the superposition of the incident electric field and the field generated by the other $\mathcal{M} - 1$ dipoles [15,16,24]. The polarizability of each dipole is given by the Clausius-Mossotti relation by using the experimental dielectric constants of the bulk material.

DDA allows for the calculation of the induced dipole moment $\mathbf{p}_i$ for each dipole i in the nanoparticle for an external electric field $\mathbf{E}^{\text{inc}}$, from which we obtain the scattered electric field generated by the $\mathcal{M}$ dipoles. Since the target molecule is placed in close proximity to the tip, the near-field expression $\mathbf{E}^{\text{NF}}$ of the scattered electric field is used [14]. The electric field generated from the nanoparticle at position $\mathbf{r}$ is thus:

$$\mathbf{E}^{\text{NF}}(\mathbf{r}) = \sum_{i=1}^{\mathcal{M}} \frac{1}{4\pi\varepsilon_0} \left(\frac{3(\mathbf{r} - \mathbf{r}_i)(\mathbf{r} - \mathbf{r}_i) \cdot \mathbf{p}_i}{|\mathbf{r} - \mathbf{r}_i|^5} - \frac{\mathbf{p}_i}{|\mathbf{r} - \mathbf{r}_i|^3} \right). \tag{3}$$

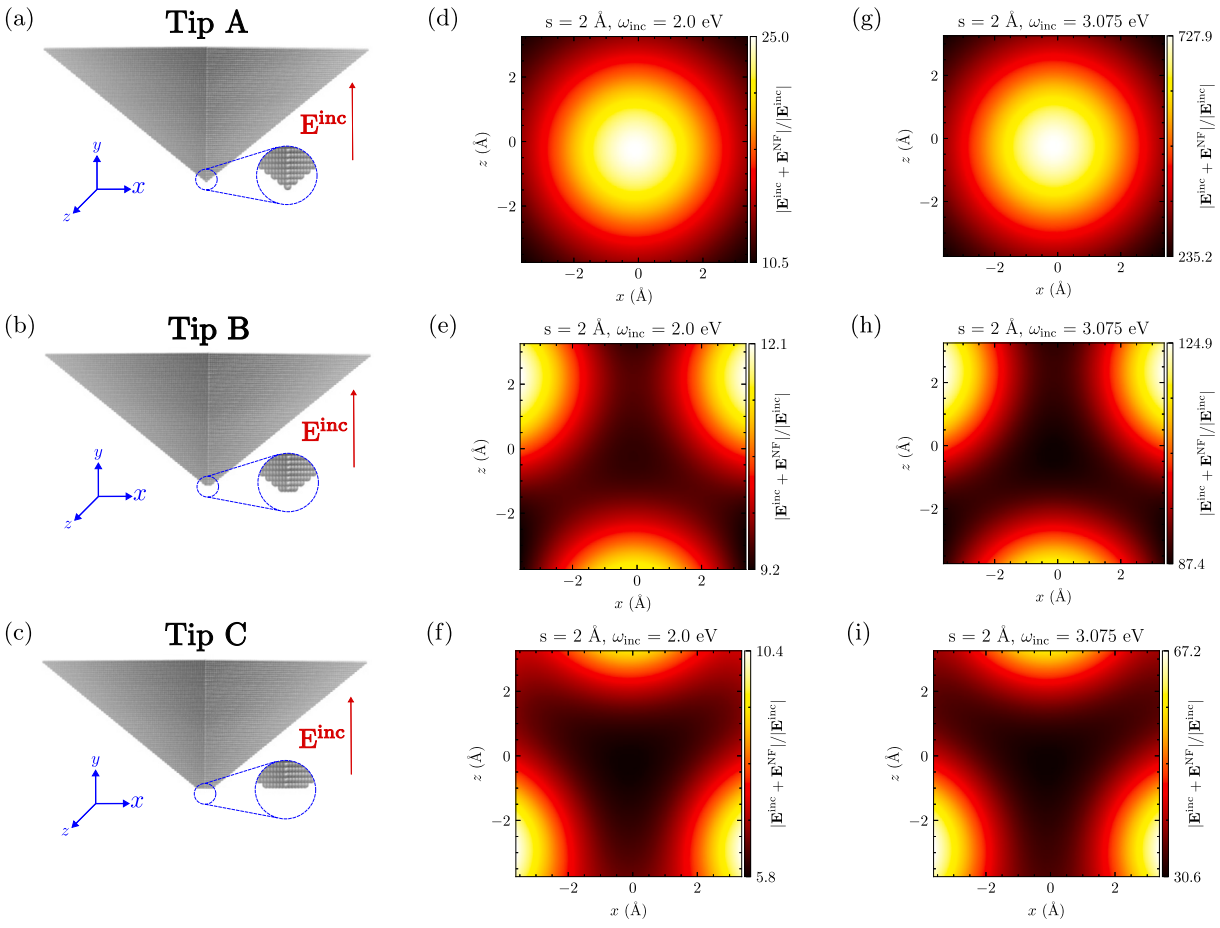

Fig. 1. (a)-(c) Atomic structures of tips A, B, and C of the nanoparticle. (d, g), (e, h), and (f, i) are plots of the electric field distribution in the $x-z$ plane for tips A, B, and C, respectively. (d)-(f) and (g)-(i) are plots of the electric field distribution at distance $s = 2$ Å below the tip for an off-resonance frequency $\omega_{\text{inc}} = 2.00$ eV and the in-resonance frequency $\omega_{\text{inc}} = 3.075$ eV, respectively. The maximum field amplitudes at the in-resonance frequency observed from the color bars (727.9, 124.9 and 67.2$|\mathbf{E}^{\text{inc}}|$ for tips A, B and C respectively) show more amplified values than those at the off-resonance frequency (25.0, 12.1, and 10.4$|\mathbf{E}^{\text{inc}}|$ for tips A, B and C respectively.)

Additionally, the absorption cross-section of the nanoparticle is calculated using the induced dipole moments and the incident field $\mathbf{E}^{\text{inc}}$ at frequency ω_{inc} as:

$$\mathrm{C}_{\text{abs}} = \frac{\omega_{\text{inc}}}{\varepsilon_0 c|\mathbf{E}^{\text{inc}}|^2}\sum_{i=1}^{\mathcal{M}}\left[\mathrm{Im}\left(\frac{\mathbf{p}_i\cdot\mathbf{p}_i^*}{\alpha_i^*}\right) - \frac{2}{3c^3}\omega_{\text{inc}}^3|\mathbf{p}_i|^2\right], \tag{4}$$

where α_i is the polarizability of the dipole $\mathbf{p}_i$ computed using the Clausius–Mossotti relation.

2.2. Raman polarizability tensor and bond polarizability method

The final key quantity needed is the Raman polarizability tensor for mode υ, expressed in Eq. (2). In a recent publication, Zhang et al. [14] have proposed to evaluate the Raman response under an inhomogeneous electric field, since it corresponds to the situation where a molecule is positioned in the vicinity of a plasmonic nanocluster. In this real-space approach, the Raman polarizability tensor is expressed as a sum over the atomic displacements rather than over the normal coordinates. The Raman polarizability tensor of the molecule ($\mathcal{N}$ atoms) can be expressed as a sum over atomic contributions:

$$\bar{\alpha}_\upsilon^{\text{Ram}} = \frac{1}{2}\left(\frac{\partial\bar{\alpha}}{\partial\mathbf{Q}_\upsilon}\right)_0\mathbf{Q}_{\upsilon 0} \tag{5}$$

$$= \frac{1}{2}\sqrt{\frac{\hbar}{\omega_\upsilon}}\sum_{l\gamma}\frac{1}{\sqrt{m_l}}\left(\frac{\partial\bar{\alpha}}{\partial u_\gamma(l)}\right)_0\chi_\gamma(l|\upsilon) \tag{6}$$

$$\equiv \sum_{l=1}^{\mathcal{N}}\bar{\alpha}_\upsilon^{(l)} \tag{7}$$

$$(\gamma = x, y, z, \quad l = 1, ..., \mathcal{N}, \quad \upsilon = 1, ..., 3\mathcal{N}),$$

where m_l is the mass of the lth atom, $u_\gamma(l)$ is the γth Cartesian displacement of the lth atom and $\chi_\gamma(l|\upsilon)$ is the γth component of the unit vector of the υth vibrational mode for the lth atom. We can now define $\bar{\alpha}_\upsilon^{(l)}$ as the atomic Raman polarizability tensor of the lth atom for the υth vibrational mode. It follows that we can express the spectrum intensity in Eq. (1) as

$$I(\omega) \propto \omega_{\text{inc}}\omega_{\text{S}}^3\sum_{\upsilon=1}^{3\mathcal{N}}(\langle n(\omega_\upsilon)\rangle + 1)\left|\boldsymbol{\eta}'\cdot\left[\sum_{l=1}^{\mathcal{N}}\bar{\alpha}_\upsilon^{(l)}\cdot\mathbf{E}(\mathbf{r}_l)\right]\right|^2\delta(\omega-\omega_\upsilon), \tag{8}$$

where $\mathbf{E}(\mathbf{r}_l) = \mathbf{E}^{\text{inc}} + \mathbf{E}^{\text{NF}}(\mathbf{r}_l)$ is the total electric field, which is the superposition of the incident field $\mathbf{E}^{\text{inc}}$ and the near-field $\mathbf{E}^{\text{NF}}(\mathbf{r}_l)$ generated from the nanoparticle on atom l of the sample located at position $\mathbf{r}_l$.

Different methods are available to calculate the derivatives of polarizability in Eq. (6). For example, Zhang et al. obtained the polarizability derivatives using a quantum chemistry package [14]. Here we adopt the bond polarizability model [17,18], as it allows for a fast and quite accurate description of the polarizability. In the BPM, the polarizability of the system $\bar{\alpha}$ is approximated as a sum over bond polarization contributions [17]:

$$\bar{\alpha} = \frac{1}{2}\left[\sum_{lB}\left\{\frac{\alpha_{\parallel}(B)+2\alpha_{\perp}(B)}{3}\right\}\bar{\mathrm{I}} + \left\{\alpha_{\parallel}(B)-\alpha_{\perp}(B)\right\}\left(\hat{\mathbf{R}}(l,B)\hat{\mathbf{R}}(l,B)-\frac{1}{3}\bar{\mathrm{I}}\right)\right] \tag{9}$$

where B points to the chemical bond connecting atom l with its neighboring atom l' and $\hat{\mathbf{R}}(l,B)$ is the corresponding unit vector from atom l to l'. $\alpha_{\parallel}(B)$ and $\alpha_{\perp}(B)$ are the static polarizabilities associated with directions parallel and perpendicular to bond B, respectively, and $\bar{\mathrm{I}}$ is the identity tensor.

Let $\mathbf{R}_0(l,B)$ be the bond vector at equilibrium, such that $\mathbf{R}(l,B) = \mathbf{R}_0(l,B) - \mathbf{u}(l)$, where $\mathbf{u}(l)$ is the displacement vector of the lth atom. From the BPM, the atomic Raman polarizability is given by

$$\begin{aligned}\bar{\alpha}_v^{(l)} = &-\frac{1}{2}\sqrt{\frac{\hbar}{\omega_v}}\frac{1}{\sqrt{m_l}}\sum_B\left[\hat{\mathbf{R}}_0(l,B)\cdot\chi(l|v)\right.\\ &\times\left\{\left(\frac{\alpha'_{\parallel}(B)+2\alpha'_{\perp}(B)}{3}\right)\bar{\mathrm{I}}+\left(\alpha'_{\parallel}(B)-\alpha'_{\perp}(B)\right)\right.\\ &\left.\times\left(\hat{\mathbf{R}}_0(l,B)\hat{\mathbf{R}}_0(l,B)-\frac{1}{3}\bar{\mathrm{I}}\right)\right\}+\left(\frac{\alpha_{\parallel}(B)-\alpha_{\perp}(B)}{R_0(l,B)}\right)\\ &\times\left\{\hat{\mathbf{R}}_0(l,B)\chi(l|v)-\chi(l|v)\hat{\mathbf{R}}_0(l,B)\right.\\ &\left.\left.-2\left(\hat{\mathbf{R}}_0(l,B)\cdot\chi(l|v)\right)\times\hat{\mathbf{R}}_0(l,B)\hat{\mathbf{R}}_0(l,B)\right\}\right],\end{aligned} \tag{10}$$

where $\alpha'_{\parallel}(B)$ and $\alpha'_{\perp}(B)$ are the radial derivatives of $\alpha_{\parallel}(B)$ and $\alpha_{\perp}(B)$ respectively, for which we use the values from Ref. [17,18] for carbon sp^2 bonds: $\alpha'_{\parallel}(B)+2\alpha'_{\perp}(B) = 7.55$ Å^2, $\alpha'_{\parallel}(B)-\alpha'_{\perp}(B) = 2.60$ Å^2 and $\alpha_{\parallel}(B)-\alpha_{\perp}(B) = 0.32$ Å^3.

3. Results

3.1. Inhomogeneous electric field of silver tips

A tetrahedron of 202,742 silver atoms obtained from the FCC crystal structure is used as a tip model for the TERS calculations performed in this study. The lattice constant of the structure is $a = 4.09$ Å and the tetrahedron is subjected to incident illumination $\mathbf{E}^{\mathrm{inc}}$ at frequency ω_{inc} in the $+y$ direction (Fig. 1.a). In DDA, the nanoparticle is sampled with a cubic mesh, where the side length of each cube (the dipole) is d. For the tetrahedron, a cubic mesh of $d = 6.063$ Å is used along with the experimental optical properties of silver from Ref. [25], to calculate the polarizability α_i of each dipole i using the Clausius-Mossotti equation, where its fit is plotted in Fig. 2.a. The absorption cross-section of the tetrahedron is also computed and plotted in Fig. 2.b, where the tetrahedron is found to be in resonance with the incident field at $\omega_{\mathrm{inc}} = 3.075$ eV.

Figs. 1.d and 1.g show the magnitude of the electric field in the $x-z$ plane at a distance $s = 2$ Å away from the tip apex at the resonance frequency $\omega_{\mathrm{inc}} = 3.075$ eV and an off-resonance frequency $\omega_{\mathrm{inc}} = 2.00$ eV. It can be observed that the field generated in the in-resonance case is much greater than that of the off-resonance case, with maximum magnitude of $727.9|\mathbf{E}^{\mathrm{inc}}|$ *vs.* $25.0|\mathbf{E}^{\mathrm{inc}}|$, respectively. Additionally, we compute the enhancement factor ($\mathcal{E}_f = (|\mathbf{E}^{\mathrm{inc}}+\mathbf{E}^{\mathrm{NF}}|/|\mathbf{E}^{\mathrm{inc}}|)^4$), which is the 4th power of the amplification of the field. The field at the center of the apex 2 Å away is found to be around $\mathcal{E}_f = 10^{11}$ (Fig. 1.g) and $\mathcal{E}_f = 10^5$ (Fig. 1.d) for $\omega_{\mathrm{inc}} = 3.075$ eV and $\omega_{\mathrm{inc}} = 2.00$ eV, respectively. As expected, the enhancement factor in the in-resonance case is much higher than the enhancement factor in the off-resonance case. Next, we evaluate the localization of the field; in other words, we calculate how fast the field decays around the tip apex. To do this, we compute the *full width at half maximum* (FWHM) in the $x-z$ plane 2 Å away from the apex. The FWHM values are 6.731 Å (Fig. 1.g) and 7.993Å (Fig. 1d.) for $\omega_{\mathrm{inc}} = 3.075$ eV and $\omega_{\mathrm{inc}} = 2.00$ eV, respectively. This indicates that the field is more localized around the tip in the in-resonance case. In conclusion, shining a monochromatic light at the plasmonic resonance frequency of the nanoparticle makes the field around it amplified and localized. In addition to the perfect tetrahedron tip morphology (we will call it *tip A*) shown in Fig. 1.a, the nanoparticle is modified by removing one and three layers from the apex of tip A to obtain tip B and tip C, respectively, whose atomic structures and the corresponding near-field magnitude plots are shown in Fig. 1. We also observe that the field is more amplified in the in-resonance case, with a maximum magnitude of $124.9|\mathbf{E}^{\mathrm{inc}}|$ for tip B and $67.2|\mathbf{E}^{\mathrm{inc}}|$ for tip C, compared with the field magnitude at the off-resonance frequency of $12.1|\mathbf{E}^{\mathrm{inc}}|$ for tip B and $10.4|\mathbf{E}^{\mathrm{inc}}|$ for tip C. Moreover, the magnitude plots show three-fold symmetry due to the atomic symmetry of the apex, which is different from the symmetry of the tetrahedron (four-fold symmetry), proving the importance of the atomic structure at the tip in describing the near-field. These modified tip models will allow investigation of how the sharpness of the tip affects the TERS spectra.

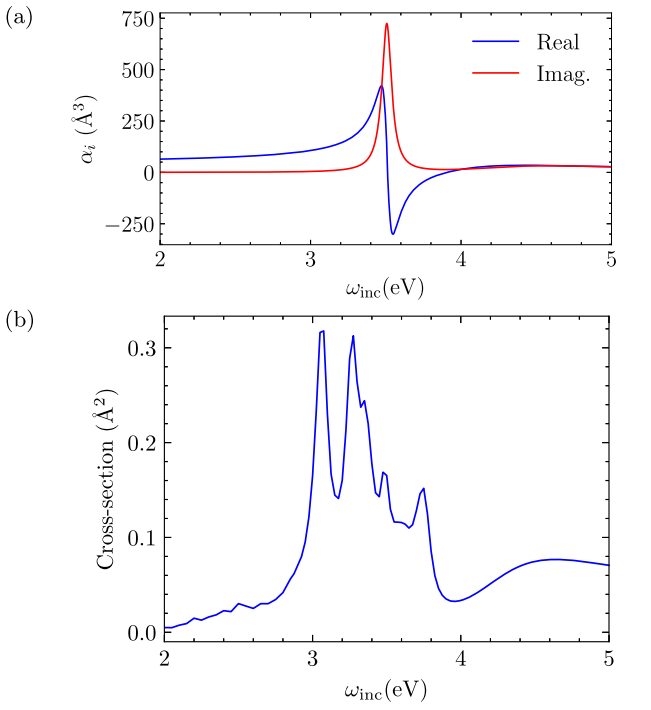

Fig. 2. (a) Real and imaginary parts of the polarizability α_i of each dipole i as a function of the incident frequency ω_{inc}. (b) The absorption spectrum of the tetrahedron nanoparticle as a function of the incident frequency ω_{inc}, where the in-resonance frequency is $\omega_{\mathrm{inc}} = 3.075$ eV. (a) and (b) are computed using a cubic mesh of $d = 6.06267$ Å and the experimental optical parameters of silver from Ref. [25].

3.2. TERS of buckminsterfullerene (C_{60})

We now compute TERS spectra using the methodology outlined above. A C_{60} molecule is placed $s = 2$ Å below the tip, where s is the distance between the tip apex and the surface of C_{60} treated geometrically as a perfect sphere. The TERS spectrum is averaged over all possible orientations of C_{60} relative to the tip, where the polarization direction of the scattered light $\boldsymbol{\eta}'$ is in the $+y$ direction. Finally, the incident electric field that polarizes the nanoparticle is in the $+y$ direction.

The simulated TERS spectrum of C_{60} is shown in Fig. 3 along with its Raman spectrum computed for a homogeneous illumination, where we compare both with the experimental results. Compared to Raman under homogeneous illumination, more modes have nonzero intensity in TERS due to the inhomogeneity of the electric field acting on C_{60}, this can be seen from Fig. 4 where the simulated TERS and Raman spectra are plotted. This highlights that Raman selection rules no longer hold in TERS as we observe nonactive Raman modes become active. The peaks corresponding to some of the nonactive Raman modes are shown

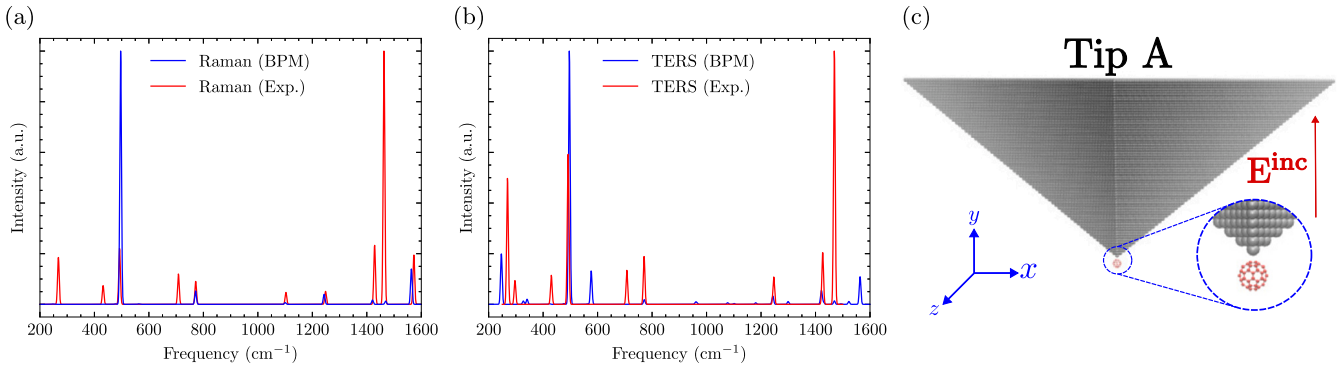

Fig. 3. (a) Raman spectrum of C_{60} where the incident electric field is homogenous. The calculation uses BPM to evaluate the polarizability derivatives, compared with the experiment in Ref. [26]. (b) TERS spectrum of C_{60} using DDA and BPM *vs.* experiment [27]. The frequency of the incident field is $\omega_{inc} = 3.075$ eV and $s = 2$ Å. (c) C_{60} placed near the tetrahedral tip. The axes of the coordinate system and the direction of the incident field are also indicated.

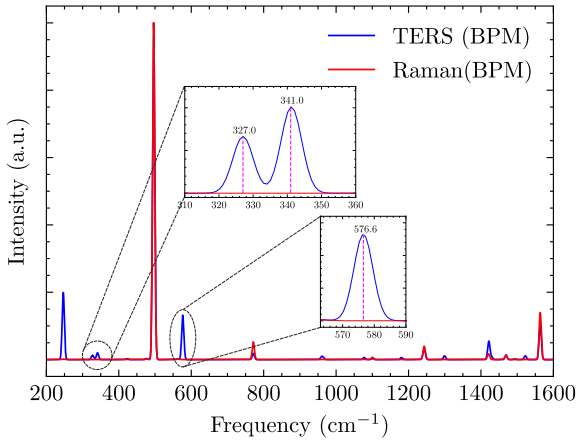

Fig. 4. Simulated TERS at $\omega_{inc} = 3.075$ eV and $s = 2$ Å. *vs.* Raman spectra of C_{60}, where three of the Raman non-active modes of frequencies 327.0 cm^{-1}, 341.0 cm^{-1} and 576.6 cm^{-1} are highlighted. These modes are shown to have non-zero intensities in the TERS spectrum, proving that the Raman selection rules are broken.

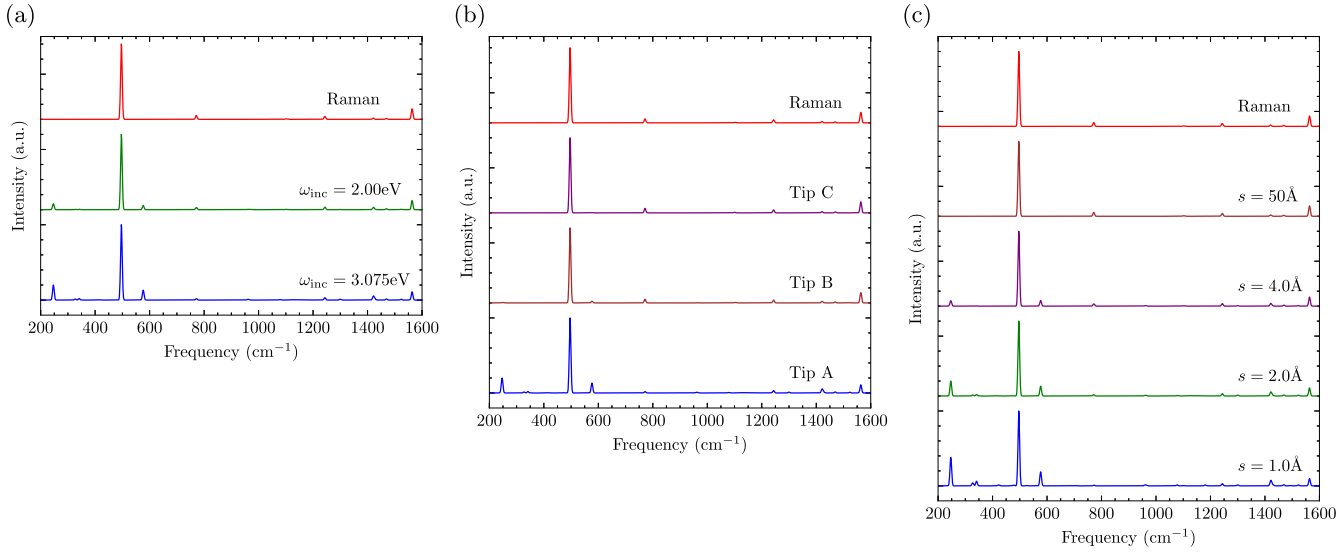

Fig. 5. (a) TERS of C_{60} at $s = 2$ Å for frequencies of the incident electric field $\omega_{inc} = 3.075$ eV and $\omega_{inc} = 2.00$ eV, where the red spectrum is the Raman spectrum with homogeneous field for reference. (b) TERS spectrum when C_{60} is placed $s = 2$ Å away from the different tips shown in Fig. 1. (c) TERS spectra for different distances from the tip: $s = 1.0$, 2.0, 4.0, and 50 Å compared with the Raman spectrum under homogeneous illumination.

in Fig. 4, at frequencies 327.0 cm^{-1}, 341.0 cm^{-1} and 576.6 cm^{-1}, where their TERS intensities are nonzero.

In Fig. 5.a, TERS is shown for different frequencies of the incident electric field. When the incident frequency is in resonance with the tip, the intensity of the modes that become active in TERS is more clearly seen. Fig. 5.b compares TERS spectra using the different tips shown in Fig. 1. As the tip becomes less sharp, the spectrum converges to the conventional Raman spectrum. It can be observed that tip A is best for computing TERS, since the field generated from it is the most localized on the individual atoms in the molecule, so the Raman nonactive modes have larger relative intensities.

Furthermore, as the tip-molecule distance increases, the intensity of the electric field becomes more homogeneous. As a result, we retrieve the conventional Raman spectrum when calculating the TERS when the molecule is sufficiently far from the tip. Fig. 5.c shows TERS at different distances from the tip. At $s = 50$ Å, the TERS signal is found to be essentially identical to the conventional Raman result: the field is homogeneous and the selection rules apply.

Finally, note that the calculations shown in Fig. 5.a indicate that compared to the conventional Raman intensities computed, the TERS spectra with tip A are enhanced by a factor of 4×10^4 and 10^2 for the in- and out-of-resonance laser frequencies. These values are in good agreement with the reported experimental results [2]. It is also noteworthy that the enhancement factor is not simply linked to the increase in the electric field to the fourth power, again highlighting the fact that localization plays a major role in the physical processes of TERS.

Table 1
Raman scans of C_{60} for multiple vibrational modes, where $\omega_{inc} = 3.075$ eV and $s = 2$ Å using tips A, B, and C shown in Fig. 1. Each plot shows the intensity as the tip scans C_{60}. 2D and 3D plots are shown for tip A, where only 2D plots are shown for tips B and C. Each row contains the plots for a different mode, labeled by the mode index and frequency.

	Tip A	Tip B	Tip C
$v = 16$, $\omega_v = 341.0 cm^{-1}$	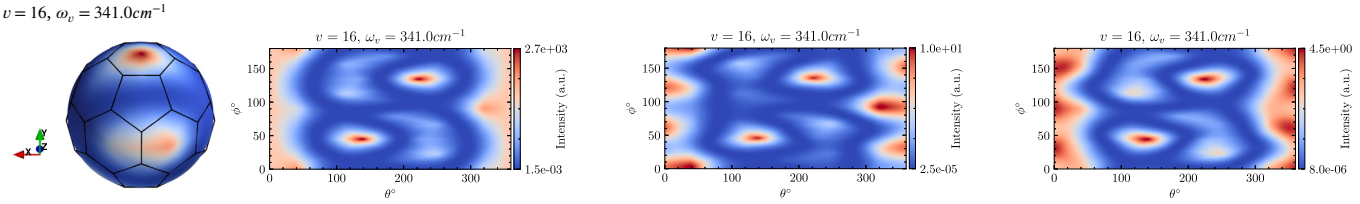		
$v = 33$, $\omega_v = 496.3 cm^{-1}$	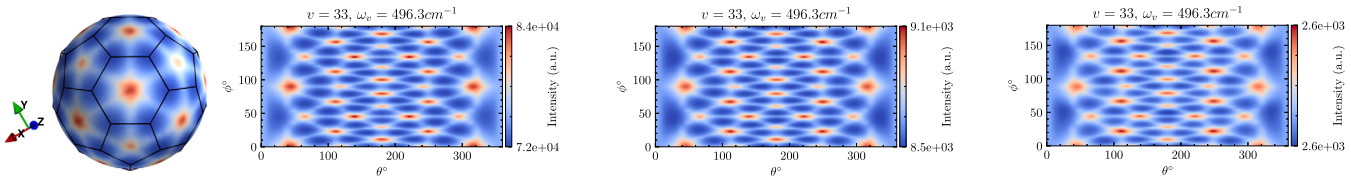		
$v = 109$, $\omega_v = 1077.6 cm^{-1}$	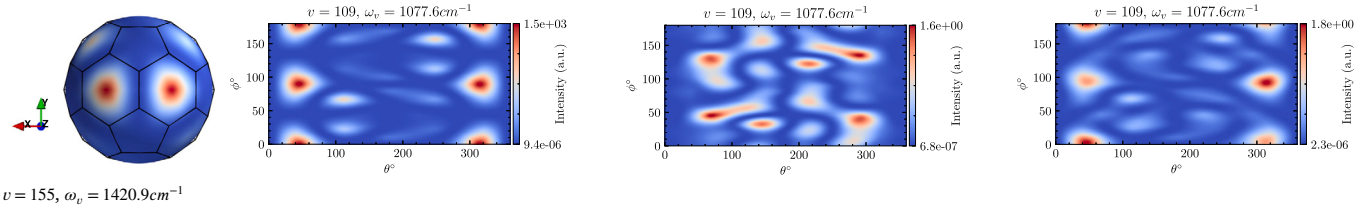		
$v = 155$, $\omega_v = 1420.9 cm^{-1}$	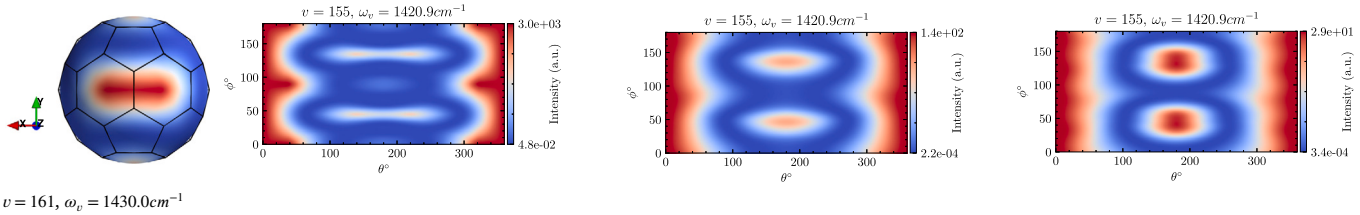		
$v = 161$, $\omega_v = 1430.0 cm^{-1}$	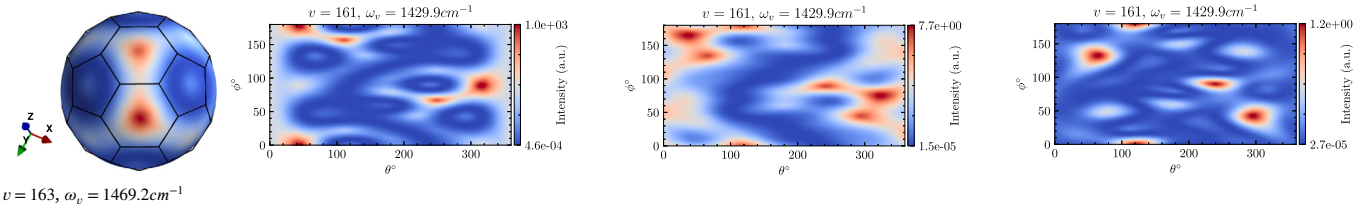		
$v = 163$, $\omega_v = 1469.2 cm^{-1}$	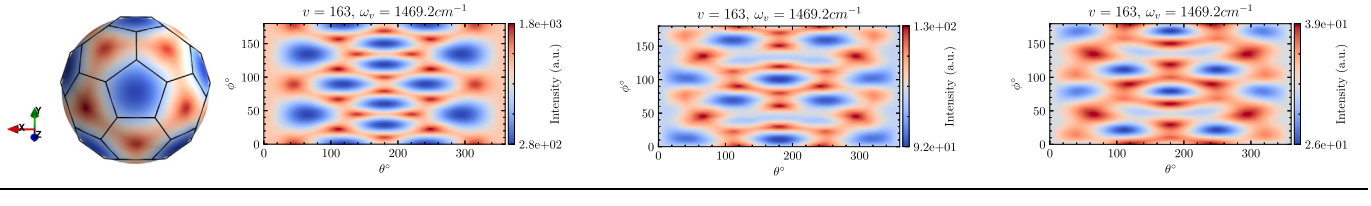		

We can also use the tip in a nano-Raman mode of operation, i.e. as a scanning probe that moves around the molecule while tracking the TERS intensity of a specific normal mode. The recorded intensity is then plotted in 2D and 3D surface plots. Table 1 shows 2D and 3D scans of C_{60} for different tips of the nanoparticle, where $\omega_{\text{inc}} = 3.075$ eV and $s = 2$ Å. There are two nondegenerate modes with symmetry A_g. The first is the radial breathing mode ($\omega_v = 496.3$ cm^{-1}), where all of the 60 carbon atoms vibrate radially in-phase with equal displacements [26]. The second is the *pentagonal pinch* mode [26] ($\omega_v = 1469.2$ cm^{-1}), where the displacements of the atoms are tangential with the expansion of the hexagonal rings and contraction of the pentagonal rings for a set of displacements [26]. From Table 1 and due to the specific symmetry of those modes, it is observed that these two modes are the ones that show the structure of C_{60} the most clearly, and they do not change much qualitatively for different tips.

4. Conclusion

We have presented a computational methodology to simulate TERS spectra in carbon nanostructures with the explicit description of the plasmonic response of the metallic tip. To calculate the local near-field at the tip apex, we used the DDA which takes into account the dielectric properties of the nanoparticle. The chosen nanoparticle is a tetrahedron with 202,742 silver atoms. By calculating the enhancement factor and the FWHM for different excitation frequencies, we observe that shining a monochromatic light with frequency in resonance with the nanoparticle generates a more localized electric field with larger enhancement.

The method is illustrated and applied to buckminsterfullerene. Comparing the TERS spectrum of C_{60} with the usual Raman spectrum, one notices that some nonactive Raman modes become active in TERS. This is due to the inhomogeneity of the field generated at the tip, which breaks the Raman selection rules. Additionally, as we remove layers from the tip, the TERS spectrum becomes more similar to the Raman spectrum, where the Raman non-active modes that can be observed in the TERS spectrum now have much lower relative intensities compared to the other peaks, confirming the advantage of using a tip with atomic-scale sharpness. The radius of curvature of tips used in TERS experiments is typically around 10 nm. This is sufficient to provide enhancement of the intensity of Raman active mode, but usually not sufficiently sharp for non-active modes to be observed. This also provides evidence of the sensitivity of the TERS spectra to the exact atomic shape of the tip at the atomic level, which further supports the picocavity effect observed experimentally [28].

We observe the convergence of the TERS spectrum with Raman as we place C_{60} far enough from the tip, where the field is no longer enhanced and localized, thereby recovering the usual Raman spectrum. Finally, multiple scans of C_{60} for various normal modes are shown, from which we gain information about the topography of the structure, which is not accessible in the usual Raman spectrum.

One key advantage of the proposed method is that it has a relatively low computational cost, in spite of the need for several computed properties such as the response of the tip to the application of an external field and the calculation of polarizability derivative. The model is found to show good accuracy and could be applied to a broad array of nanoscale systems. Note that regarding the order light interacts with the sample and the tip [29], we only consider S (Sample) and TS (Tip-Sample) terms and not the potential influence of the sample (molecule) on the tip. Moreover, spatial field interference is not considered in our treatment since we are interested in computing Raman for small molecules. It can be included by adding a position-dependent exponential term in Eq. (8) to consider the interference between the Raman sources. This effect is more important in extended systems such as graphene, where the spatial field interference is crucial in evaluating TERS, as it causes different field enhancements depending on the symmetry of different modes [30,31].

Declaration of competing interest

The authors declare that they have no known competing financial interests or personal relationships that could have appeared to influence the work reported in this paper.

Data availability

Data will be made available on request.

Acknowledgements

MF and VM acknowledge the support of the Focus Center at Rensselaer Polytechnic Institute, a NYS Department of Economic Development award (No. A21-0125-002 and RPI designation A50634.2326). LH acknowledges the support of the ARC (Actions de recherche concertées) research project No. 19/24-102 SURFASCOPE.

References

[1] J. Langer, D.J. de Aberasturi, J. Aizpurua, R.A. Alvarez-Puebla, B. Auguié, J.J. Baumberg, G.C. Bazan, S.E.J. Bell, A. Boisen, A.G. Brolo, J. Choo, D. Cialla-May, V. Deckert, L. Fabris, K. Faulds, F.J.G. de Abajo, R. Goodacre, D. Graham, A.J. Haes, C.L. Haynes, C. Huck, T. Itoh, M. Käll, J. Kneipp, N.A. Kotov, H. Kuang, E.C.L. Ru, H.K. Lee, J.-F. Li, X.Y. Ling, S.A. Maier, T. Mayerhöfer, M. Moskovits, K. Murakoshi, J.-M. Nam, S. Nie, Y. Ozaki, I. Pastoriza-Santos, J. Perez-Juste, J. Popp, A. Pucci, S. Reich, B. Ren, G.C. Schatz, T. Shegai, S. Schlücker, L.-L. Tay, K.G. Thomas, Z.-Q. Tian, R.P.V. Duyne, T. Vo-Dinh, Y. Wang, K.A. Willets, C. Xu, H. Xu, Y. Xu, Y.S. Yamamoto, B. Zhao, L.M. Liz-Marzán, Present and future of surface-enhanced raman scattering, ACS Nano 14 (2020) 28.

[2] P. Verma, Tip-enhanced raman spectroscopy: technique and recent advances, Chem. Rev. 117 (2017) 6447.

[3] R. Rani, A. Yoshimura, S. Das, M.R. Sahoo, A. Kundu, K.K. Sahu, V. Meunier, S.K. Nayak, N. Koratkar, K.S. Hazra, Sculpting artificial edges in monolayer mos_2 for controlled formation of surface-enhanced raman hotspots, ACS Nano 14 (6258) (2020), pMID: 32330006, https://doi.org/10.1021/acsnano.0c02418.

[4] S. Huang, X. Ling, L. Liang, Y. Song, W. Fang, J. Zhang, J. Kong, V. Meunier, M.S. Dresselhaus, Molecular selectivity of graphene-enhanced raman scattering, Nano Lett. 15 (2015) 2892, pMID: 25821897, https://doi.org/10.1021/nl5045988.

[5] G. Binnig, H. Rohrer, C. Gerber, E. Weibel, Surface studies by scanning tunneling microscopy, Phys. Rev. Lett. 49 (1982) 57.

[6] G. Binnig, C.F. Quate, C. Gerber, Atomic force microscope, Phys. Rev. Lett. 56 (1986) 930.

[7] A.C. Gadelha, D.A.A. Ohlberg, C. Rabelo, E.G.S. Neto, T.L. Vasconcelos, J.L. Campos, J.S. Lemos, V. Ornelas, D. Miranda, R. Nadas, F.C. Santana, K. Watanabe, T. Taniguchi, B. van Troeye, M. Lamparski, V. Meunier, V.-H. Nguyen, D. Paszko, J.-C. Charlier, L.C. Campos, L.G. Cançado, G. Medeiros-Ribeiro, A. Jorio, Localization of lattice dynamics in low-angle twisted bilayer graphene, Nature 590 (2021) 405.

[8] R.M. Stöckle, Y.D. Suh, V. Deckert, R. Zenobi, Nanoscale chemical analysis by tip-enhanced raman spectroscopy, Chem. Phys. Lett. 318 (2000) 131.

[9] M.S. Anderson, Locally enhanced raman spectroscopy with an atomic force microscope, Appl. Phys. Lett. 76 (2000) 3130.

[10] B. Pettinger, G. Picardi, R. Schuster, G. Ertl, Surface enhanced raman spectroscopy: towards single molecule spectroscopy, Electrochemistry 68 (2000) 942.

[11] N. Hayazawa, Y. Inouye, Z. Sekkat, S. Kawata, Metallized tip amplification of near-field raman scattering, Opt. Commun. 183 (2000) 333.

[12] M. Moskovits, D.P. DiLella, K.J. Maynard, Surface raman spectroscopy of a number of cyclic aromatic molecules adsorbed on silver: selection rules and molecular reorientation, Langmuir 4 (1988) 67.

[13] P. Liu, D.V. Chulhai, L. Jensen, Single-molecule imaging using atomistic near-field tip-enhanced raman spectroscopy, ACS Nano 11 (2017) 5094.

[14] Y. Zhang, Z. Dong, J. Aizpurua, Theoretical treatment of single-molecule scanning raman picoscopy in strongly inhomogeneous near fields, J. Raman Spectrosc. 52 (2021) 296.

[15] B.T. Draine, The discrete-dipole approximation and its application to interstellar graphite grains, Astrophys. J. 333 (1988) 848.

[16] E.M. Purcell, C.R. Pennypacker, Scattering and absorption of light by nonspherical dielectric grains, Astrophys. J. 186 (1973) 705.

[17] R. Saito, M. Furukawa, G. Dresselhaus, M.S. Dresselhaus, Raman spectra of graphene ribbons, J. Phys. Condens. Matter 22 (2010) 334203.

[18] S. Guha, J. Menéndez, J.B. Page, G.B. Adams, Empirical bond polarizability model for fullerenes, Phys. Rev. B 53 (1996) 13106.

[19] A. Togo, I. Tanaka, First principles phonon calculations in materials science, Scr. Mater. 108 (2015) 1.

[20] J.J. Mortensen, L.B. Hansen, K.W. Jacobsen, Real-space grid implementation of the projector augmented wave method, Phys. Rev. B 71 (2005) 035109.

[21] J. Enkovaara, C. Rostgaard, J.J. Mortensen, J. Chen, M. Dułak, L. Ferrighi, J. Gavnholt, C. Glinsvad, V. Haikola, H.A. Hansen, H.H. Kristoffersen, M. Kuisma, A.H. Larsen, L. Lehtovaara, M. Ljungberg, O. Lopez-Acevedo, P.G. Moses, J. Ojanen, T. Olsen, V. Petzold, N.A. Romero, J. Stausholm-Møller, M. Strange, G.A. Tritsaris, M. Vanin, M. Walter, B. Hammer, H. Häkkinen, G.K.H. Madsen, R.M. Nieminen, J.K. Nørskov, M. Puska, T.T. Rantala, J. Schiøtz, K.S. Thygesen, K.W. Jacobsen, Electronic structure calculations with gpaw: a real-space implementation of the projector augmented-wave method, J. Phys. Condens. Matter 22 (2010) 253202.

[22] A.H. Larsen, J.J. Mortensen, J. Blomqvist, I.E. Castelli, R. Christensen, M. Dułak, J. Friis, M.N. Groves, B. Hammer, C. Hargus, E.D. Hermes, P.C. Jennings, P.B. Jensen, J. Kermode, J.R. Kitchin, E.L. Kolsbjerg, J. Kubal, K. Kaasbjerg, S. Lysgaard, J.B. Maronsson, T. Maxson, T. Olsen, L. Pastewka, A. Peterson, C. Rostgaard, J. Schiøtz, O. Schütt, M. Strange, K.S. Thygesen, T. Vegge, L. Vilhelmsen, M. Walter, Z. Zeng, K.W. Jacobsen, The atomic simulation environment—a python library for working with atoms, J. Phys. Condens. Matter 29 (2017) 273002.

[23] J.P. Perdew, K. Burke, M. Ernzerhof, Generalized gradient approximation made simple, Phys. Rev. Lett. 77 (1996) 3865.

[24] M.S.N. Navrood, Theoretical study of localized surface plasmons of metal nanoparticles, clusters and embedded metal nanoparticles in matrices, 2009.

[25] H.U. Yang, J. D'Archangel, M.L. Sundheimer, E. Tucker, G.D. Boreman, M.B. Raschke, Optical dielectric function of silver, Phys. Rev. B 91 (2015) 235137.

[26] M.S. Dresselhaus, G. Dresselhaus, P.C. Eklund, Raman scattering in fullerenes, J. Raman Spectrosc. 27 (1996) 351.

[27] P. Verma, K. Yamada, H. Watanabe, Y. Inouye, S. Kawata, Near-field raman scattering investigation of tip effects on c_{60} molecules, Phys. Rev. B 73 (2006) 045416.

[28] F. Benz, M.K. Schmidt, A. Dreismann, R. Chikkaraddy, Y. Zhang, A. Demetriadou, C. Carnegie, H. Ohadi, B. de Nijs, R. Esteban, J. Aizpurua, J.J. Baumberg, Single-molecule optomechanics in picocavities, Science 354 (2016) 726, https://www.science.org/doi/pdf/10.1126/science.aah5243.

[29] L. Novotny, B. Hecht, Principles of Nano-Optics, 2nd ed., Cambridge University Press, 2012.

[30] L.G. Cançado, R. Beams, A. Jorio, L. Novotny, Theory of spatial coherence in near-field raman scattering, Phys. Rev. X 4 (2014) 031054.

[31] R. Beams, L.G. Cançado, S.-H. Oh, A. Jorio, L. Novotny, Spatial coherence in near-field raman scattering, Phys. Rev. Lett. 113 (2014) 186101.